Data reduction methods for flow tagging velocity measurements

R. B. Hill, J. C. Klewicki

Abstract Data reduction algorithms for flow tagging velocity measurements are presented. Laser induced photochemical anemometry (LIPA) is the flow tagging technique used for the current experiments. This technique yields temporally and spatially resolved velocity and vorticity information. LIPA is first demonstrated in a laminar boundary layer. More complicated applications include a laminar boundary layer interacting with a flush-mounted, rotating disc, as well as a shear wake interaction with a circular cylinder. Advancements of the current study include the use of improved photoluminescent chemicals, as well as implementation of accurate image processing/data reduction algorithms. These yield typical errors in the instantaneous velocity data of less than 4%.

1
Introduction

Laser induced photochemical anemometry (LIPA) entails the use of a laser and a light sensitive chemical for the purpose of qualitative and quantitative flow field analysis. Many innovations, in terms of light sources and chemicals used, have advanced this measurement technique greatly.

The use of light sensitive chemicals for the purposes of fluid mechanics research was, to the author's knowledge, first introduced by Miller (1962). In this study he utilized flash photolysis, which uses a flash tube to excite a photochromic chemical, as a means of flow visualization. This technique was used (Goldfish et al. 1965) as a way to non intrusively add a "dye" to the flow field at any desired location. Popovich and Hummel (1967) were the first to extend flash photolysis flow visualization to a velocity measurement technique. A primary contribution of their work was to reduce the size of the region excited by the light source such that it formed a thin line that could be used in measuring velocities. Works by Popovich

(1969) and Popovich and Lavallee (1970) attempted to use this technique in turbulent flow fields with limited success. A later study (Seeley et al. 1975) of laminar flow around a sphere shows instantaneous errors in velocity measurements of 5% in the free stream and 13% near the sphere. Since the earlier studies were done in the demanding environment of the near-wall region of turbulent boundary layers, it is likely that many aspects of their measurements were more indicative of experimental error than the properties of the flow.

The introduction of the pulsed excimer laser to photochemical flow measurements (e.g. Falco and Chu 1987) led to the current acronym, LIPA. Since these pioneering works, numerous researchers have used photochromic chemicals for the purposes of flow field analysis (e.g. Ojha et al. 1989; Chu and Liao 1992). Similar laser based flow tagging techniques have also been introduced by Miles et al. (1987) for high speed gas flows, and Lempert (1992) in liquids (using caged fluorescein dye rather than photochromic chemicals). The work by Falco and Chu, however, was the first to use two sets of intersecting lines to form a grid. This grid technique allowed two components of velocity to be measured over a planar domain. More recently, Gendrich et al. (1994) have used photoluminescent chemicals for the study of flow velocities as well as mixing and reaction.

The present study advances the LIPA technique through the use of long emission, high light yielding photoluminescent chemicals (Ponce et al. 1993), as a means to "tag" the grid or lines in the fluid. Significant advancements have also been made in efficient data reduction algorithms which compute velocity information from multiple line or grid images. In the following section the LIPA technique is described. Section 3 then describes the data reduction algorithms for two different flow tagging schemes. Section 4 gives a detailed error analysis associated with the measured velocities. Sections 5 and 6 describe the particular experimental parameters used for this study and present sample results. Section 7 then draws conclusions from the study.

R. B. Hill, J. C. Klewicki
Physical Fluid Dynamics Laboratory
Department of Mechanical Engineering
3209 MEB
University of Utah
Salt Lake City, Utah 84112, USA

Correspondence to: R. B. Hill

2
Laser induced photochemical anemometry

LIPA is a non-intrusive time resolved method of measuring velocities over a planar domain. Depending on the optical configuration, LIPA can yield instantaneous velocity, vorticity, and strain rate information over that domain.

LIPA, conceptually and in practice, is straightforward. The flow field of interest is first doped with a small concentration (typically a 10^{-4} M solution) of one of the following types of photochemical. Photochromic chemicals have the property

that when excited by UV light their absorption and reflection spectra change. This produces a color change for some short duration. This duration ranges from a few milliseconds to several seconds, depending on the specific photochromic chemical. Phosphorescent chemicals have the property that when exposed to UV light they become excited to a higher energy level. As the molecules rapidly return to their unexcited state, this energy is emitted as light which is (in this case) in the visible spectrum. Phosphorescent emission lifetimes are typically much shorter than photochromic durations, ranging from a few nanoseconds to several milliseconds.

The present research utilizes a phosphorescent chemical (1-BrNp·Gβ-CD·ROH ternary complex) recently developed by Ponce et al. (1993). This chemical is superior to previously used chemicals for several reasons. The chemical completely dissolves in water, eliminating scattered light that is a common problem with chemicals in suspension in the fluid. The light level emitted is higher than that of previous chemicals, and the usable life of the chemical is excellent; the present research has utilized the same "batch" for over a year with very little degradation in terms of emitted light. This results from the fact that the chemical can be "recharged" by simply adding more alcohol to the system. Furthermore, unlike the so-called caged fluorescein dyes, the excitation/emission process is reversible and requires only a single laser.

At present, two different optical configurations are used to excite the dissolved photochemical. These are the grid and multiple line configurations discussed below.

2.1
Grids

In the grid technique, a pulsed ultraviolet laser beam is divided into two sets of laser lines which intersect to form a grid. This is achieved through the use of a beamsplitter and two beam dividers (Fig. 1). The grid is then allowed to deform (as a result of the fluid flow) for a few milliseconds at which time a

synchronized CCD camera shutters capturing the deformed grid on video. The distance that the intersection traveled $(\Delta x, \Delta y)$ is measured by comparing the undeformed and deformed grids. By using $V \approx (\Delta x/\Delta t\, i + \Delta y/\Delta t\, j)$, where Δt is the deformation time (i.e. the time between the laser firing and the camera shuttering), the two components of velocity at each intersection are calculated (Fig. 2). From these velocities, four velocity gradients, one component of vorticity, and at least one component of the rate of strain can be calculated. Figure 3 shows a typical deformed grid image.

2.2
Multiple lines

For flowfields dominated by a single velocity component (see Sect. 4.3), the multiple line technique can be used to instantaneously measure single component velocity profiles over a planar domain. In this adaptation, instead of generating a grid, the laser light is configured into a series of coplanar, approximately parallel lines. By pointwise subtraction of the undeformed lines (Fig. 4a) from the corresponding deformed
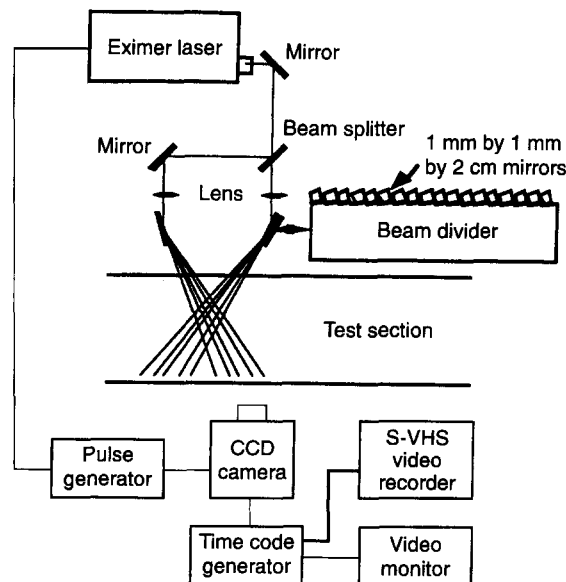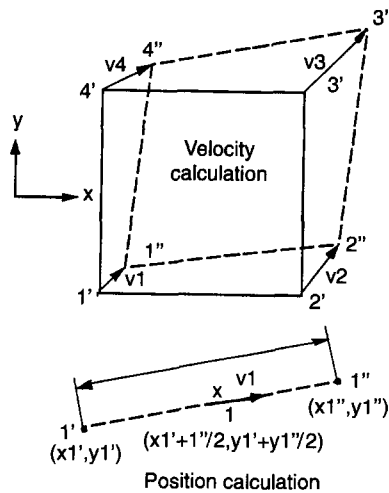
Fig. 2. Velocity and position calculation for LIPA grid technique
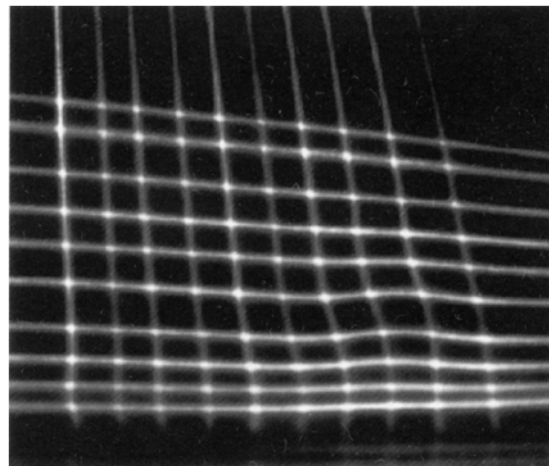
Fig. 1. LIPA optical configuration

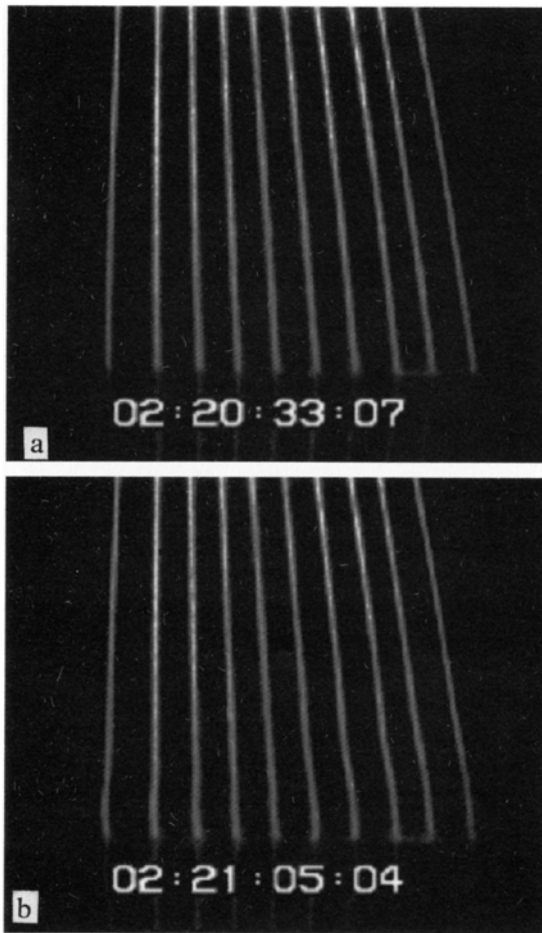Fig. 3. Typical deformed LIPA grid image

Fig. 4. a Typical undeformed multiple line LIPA image; **b** typical deformed multiple line LIPA image

lines (Fig. 4b), the velocity as well as two velocity gradients at each point can be calculated. This line-based technique naturally provides velocity profile information that is often more easily interpreted than other types of data representation.

3
Image processing methodology

3.1
Overview

Both the multiple line and the grid reduction methods rely on the same line center locating technique. In either case, both deformed and undeformed images (lines or grids) are digitized at 640×480 pixels. The undeformed images (typically 64 frames) are then ensemble averaged to yield a robust measure of the initial ($t = t_0$) line or grid positions. The deformed ($t = \Delta t$) lines or grids are then located at each instant. Subtraction of the undeformed images from the deformed images then yields the deformation over the prescribed Δt. Because this Δt is small relative to the time scales of the flow, a Lagrangian approximation can be used to determine velocities.

3.2
Multiple lines

The first step in the multiple line data reduction process involves calculating the x position associated with each y location along the undeformed laser lines. To do this, a region of interest (ROI) enclosing each laser line (e.g. a narrow parallelogram) is first defined. At each y position for each line, a variable pass Gaussian smoothing routine is applied to the intensity versus position curve over the ROI and transverse to the laser line. Figure 5 shows both the raw and the smoothed curves. The maximum intensity, $I_{\max}$ (lowest greyscale value), pixel location is then found from the smoothed points. A second order least squares curve fit consisting of a number of (typically 5–9) x versus I points is applied to the smoothed intensity data in the region surrounding this peak location. The derivative of this fit is then evaluated to find the maximum intensity which corresponds to the line center. The advantages of this two step procedure are further discussed in Sect. 4. The next step of the data reduction is to average the x positions from a number of video frames (typically 64) to give a robust description of the t_0 set of lines.

The velocities at each y position along each line are now calculated from the time equals Δt images. This involves first finding the positions of the distorted lines in the same way that the t_0 lines were found. The x positions for the t_0 lines are read in and subtracted from the x positions from the distorted lines giving Δx values. By multiplying these by the appropriate factors ($1/\Delta t$ and a meters/pixel conversion) the velocity at each y location on each line is found.

3.3
Grids

The reduction of data from grid images is very similar to the reduction of multiple line data. However, instead of tracking points along a line, the intersections of two lines are tracked. The first step in the grid data reduction displays the major difference between the image processing method for lines and for grids. The approximate positions of each of the intersection points are first manually determined. At each intersection, the four neighboring intersections are used to determine the nominal directions of the laser lines defining the intersection. For each of these four directions, a distance is traversed a specified distance outward from the intersection. This distance is made large enough to avoid the often complicated intensity variations within the intersection region. This procedure defines a single point (nominally on each of the four lines) that lie a fraction of the distance to the neighboring intersections away from the intersection of interest (see Fig. 6). At each of these four points, a region of interest is defined that is nominally perpendicular to the laser lines.

The second part of the method then works on the ROI's to find the line centers in the same manner as for multiple lines. This locates the line center at a point on each of the four lines surrounding the intersection of interest. These four x, y locations are divided into two "opposing" pairs, each defining a line segment through the intersection region. The point of intersection of these two line segments is defined as the center of the LIPA grid intersection. By using this approach, we have eliminated the problem of dealing with the actual intersection
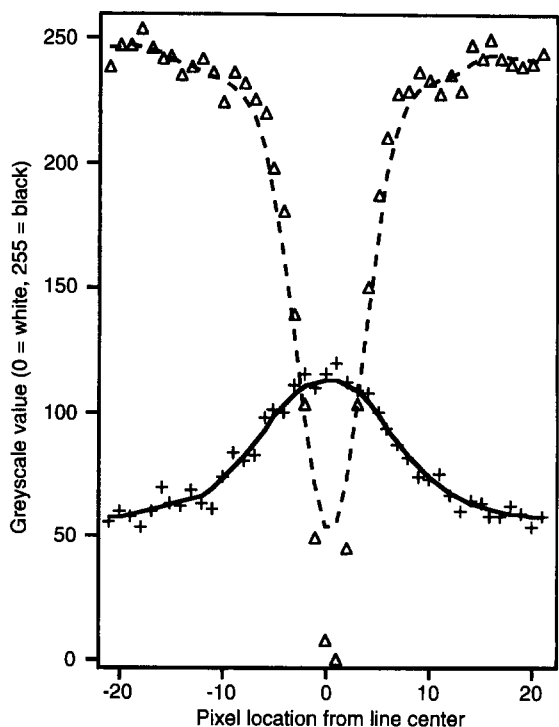
Fig. 5. Greyscale intensity versus pixel location (+ raw photochromic; —— smoothed photochromic; △ raw photoluminescent; – – – smoothed photoluminescent)
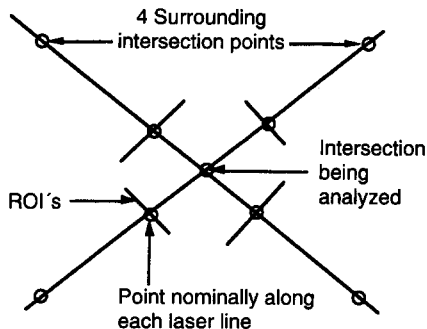

Fig. 6. Region of interest for grid area

region which can be quite complicated and of poor image quality (e.g. the region is often saturated as the light emitted from both lines is summed). In effect, the problem is reduced to something very similar to the multiple line data reduction.

The instantaneous velocities at each grid intersection point are calculated by subtracting the averaged x and y locations of the undeformed grid intersections from the instantaneous x and y locations of the deformed grid intersections (yielding Δx and Δy values). From these differences, the instantaneous u and v components of velocity at each point are determined.

4
Error analysis
The error analysis is divided into errors associated with the finite length and time scales of the measurements, and uncertainties in the quantification of these lengths and times.

Additional error analysis is provided for applications involving three dimensional flowfields, and in particular, turbulent wall-bounded shear flows. For the purposes of illustration, we use the actual parameters from our current experiments. The resultant error estimates therefore reflect the actual accuracy of typical LIPA experiments.

4.1
Errors of first order approximation for velocity
For the current perturbed laminar boundary layer experiments (see Sect. 6), the viscosity was measured to be 7.2×10^{-6} m²/s, and the velocity gradient at the wall, 30.0 s^{-1}. This gives a viscous length scale of $l^+ = 0.49$ mm, and a viscous time scale of $t^+ = 33.3$ ms. Laser line deformations were less than 0.5 mm for delay times of approximately 7 ms. This gives a maximum deformation of just over one viscous length scale and a deformation time of less than a quarter of a viscous time scale.

4.2
Measurement errors
The actual errors in the data come fom several sources. There are errors associated with the velocity as well as the positions at which those velocities are measured. Velocity components are determined by:

$$V \approx \frac{\Delta x}{\Delta t} = \frac{(x_2 - x_1)c}{\Delta t}, \tag{1}$$

where c is a conversion having the units of m/pixel. In the following, the errors associated with the length scale conversion factor and the delay time, Δt are discussed first. The errors (relative to our image processing algorithm) associated with finding the x locations at each point along each line are then quantified.

Typical errors associated with the terms in the above expression for velocity are $\Delta t = \Delta t \pm \delta \Delta t$, with $\Delta t = 7.17$ ms, and $\delta \Delta t = 0.05$ ms. This error estimate results from a CCD exposure time of approximately 0.5 ms. It is reduced to 0.05 ms because information regarding the exponential decay rate of the luminescence is known. The conversion factor, c, is given by $c = c \pm \delta c$, with $c = 0.0000858$ m/pixel and $\delta c = 7.33 \times 10^{-7}$ m/pixel from standard error analysis (e.g. Taylor 1982).

A seven pass Gaussian smoothing routine followed by a seven point least squares fit were employed for the present experiments. These values were chosen to minimize x position deviations with respect to an ensemble averaged line, as well as minimize mean data bias. This data bias completely results from the laser line not being exactly perpendicular to the ROI lines used to analyze it. Methods for further reducing this bias are currently being explored. Table 1 shows the standard deviation and mean bias as a function of the number of passes for the Gaussian smoothing routine and the number of points for the least squares curve fit. This table shows that as each of these parameters increase, the standard deviation decreases, but the amount of mean bias increases. The parameter values chosen yield a standard deviation of 0.3531 pixels, and 0.079 pixels of mean bias. For the present work, the bias is further reduced to unquantifiable levels as the mean flow is

Table 1. Standard deviation (upper value) and mean data bias (lower value) as a function of points in least squares curve fit and number of Gaussian smoothing routine passes. Box denotes parameters used in the current experiments

	ls5	ls7	ls9	ls11	ls13	ls15
n pass1	0.4767	0.4298	0.3908	0.3570	0.3256	0.3065
	−0.0128	0.0179	0.0549	0.0887	0.1206	0.1510
n pass2	0.4462	0.4103	0.3769	0.3439	0.3115	0.2866
	0.0032	0.0326	0.0627	0.0932	0.1244	0.1521
n pass3	0.4256	0.3955	0.3650	0.3344	0.3058	0.2833
	0.0197	0.0442	0.0730	0.1018	0.1300	0.1574
n pass4	0.4108	0.3843	0.3563	0.3276	0.3005	0.2799
	0.0311	0.0547	0.0805	0.1073	0.1350	0.1609
n pass5	0.3974	0.3736	0.3480	0.3219	0.2971	0.2779
	0.0415	0.0638	0.0883	0.1144	0.1405	0.1649
n pass6	0.3849	0.3626	0.3389	0.3153	0.2934	0.2759
	0.0515	0.0714	0.0943	0.1190	0.1449	0.1701
n pass7	0.3732	0.3531	0.3314	0.3099	0.2904	0.2752
	0.0602	0.0792	0.1019	0.1257	0.1503	0.1729
n pass8	0.3636	0.3451	0.3251	0.3054	0.2877	0.2740
	0.0690	0.0865	0.1082	0.1321	0.1559	0.1788
n pass9	0.3549	0.3371	0.3191	0.3013	0.2848	0.2726
	0.0766	0.0929	0.1148	0.1373	0.1605	0.1842
n pass10	0.3466	0.3306	0.3135	0.2969	0.2820	0.2709
	0.0846	0.1009	0.1214	0.1432	0.1656	0.1880
n pass11	0.3391	0.3245	0.3083	0.2929	0.2795	0.2691
	0.0910	0.1076	0.1271	0.1485	0.1702	0.1909
n pass12	0.3320	0.3184	0.3032	0.2891	0.2770	0.2677
	0.0973	0.1137	0.1330	0.1531	0.1736	0.1939
n pass13	0.3259	0.3128	0.2988	0.2858	0.2748	0.2664
	0.1049	0.1208	0.1377	0.1572	0.1777	0.1977

subtracted from the perturbed flow (to be discussed further in Sect. 6).

The indicated standard deviation (error) contributes to the velocity calculation of Eq. (1) as $x_1 = x_1 \pm \delta x_1$ with $\delta x_1 = 0.3531/8.0 = 0.0441$ pixels (with the factor of 8 coming from the fact that the undeformed x locations are averaged over 64 frames (Taylor 1982)), and $x_2 = x_2 \pm \delta x_2$ with $\delta x_2 = 0.3531$ pixels. A 10 pixel deformation of the laser line is typical. In this case, the error in the instantaneous velocity is $V = V \pm \delta V$ with $V = 0.120$ m/s and $\delta V = 0.0047$ m/s or 3.7%. For the perturbed boundary layer experiments, these velocities were then ensemble averaged over nine realizations, and therefore yield $V = 0.120$ m/s and $\delta V = 0.0016$ m/s or a 1.3% error.

A separate error analysis for the x and y positions (locating the velocity) is not presented here as these errors are of the same order as the errors in the length scales of the velocities (approx. 0.35 pixels or 0.031 mm). Curvature effects from the photographic optics can also be neglected. This is appropriate because for the velocity calculations, we are finding the difference between two points that are nominally ten pixels apart. Over this distance, the curvature effect is of order 0.01 pixel. Regarding absolute position calculations (for the purposes of locating the measurements relative to the test section, for example), the picture distortion is nominally 0.01 pixel/pixel. Given a worst case scenario, this error could reach 5 pixels, or approximately 0.4 mm.

Most aspects of the multiple line error analysis are also valid for the grid images. For example, the error in locating the four points surrounding the intersection of interest is identical to the error in finding the x positions of the lines. The errors in finding the length scale conversion factor and the delay time are also identical. If the distorted phosphorescent line is assumed linear over the length of the curve fit (a valid approximation as line segment lengths are typically less than a single viscous length scale), an upper bound on the standard deviation of the x and y positions of the laser line intersection is given by the standard deviation in finding the line centers themselves. Calculations have actually shown that the error is reduced to 0.267 pixel compared to 0.353 pixel for a single line. This is due to the fact that the random errors on each of the four line segments, on average, tend to offset each other.

4.3
Multiple line method errors due to flow tangential to the lines

The multiple line technique is susceptible to additional errors associated with velocities parallel to the laser lines. These errors result from the inability to identify and subsequently track unique fluid elements. To estimate these errors, an understanding of the flow field is necessary. In particular, for flow fields in which the component of velocity tangent to the line is significant relative to the velocity normal to the line, and a significant gradient along the line exists, the errors associated
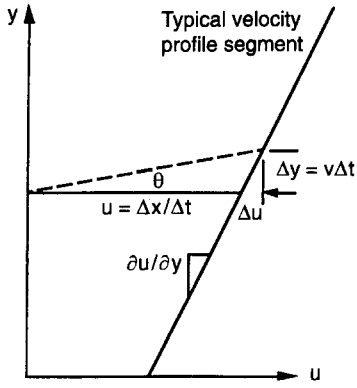
Fig. 7. Schematic of how a velocity tangent to a LIPA line can generate an error in the velocity normal to the line

with the multiple line technique become substantial. For these flowfields, the grid technique is a more appropriate choice.

Because of the large mean shear near the surface, wall-bounded turbulent flows represent a demanding environment for the line technique. Figure 7 depicts how v velocities can induce errors in the u component. From this figure it is seen that the error in the streamwise velocity u is:

$$\Delta u^+ = \Delta y^+ \left(\frac{\partial u}{\partial y}\right)^+ = v^+ \Delta t^+ \left(\frac{\partial u}{\partial y}\right)^+, \tag{2}$$

or as a percentage of the instataneous velocity,

$$\frac{\Delta u}{u} = \Delta t \left(\frac{v}{u}\frac{\partial u}{\partial y}\right), \tag{3}$$

where v, u, and $\partial u/\partial y$ are instantaneous quantities, and Δt is the LIPA time delay. Equation (3) indicates that the percent error in the instantaneous streamwise velocity is proportional to the instantaneous inplane flow angle, $\theta = \tan^{-1}(v/u)$, and the instantaneous gradient of u along the line.

Equation (3) provides a means by which to assess this source of error in the multiple line technique. To this end, the spatially and temporally resolved 4-element hot-wire data of Klewicki (1989) were used to generate pdfs of this error at various locations from the wall in turbulent boundary layer flows. For example, Fig. 8a is the pdf of $(v/u)\partial u/\partial y$ at $y^+ = 15.6$, $R_\theta = 2870$. This pdf was generated directly from time series data of u, v, and $\partial u/\partial y$ according to Eq. (3). The $(v/u)\partial u/\partial y$ values corresponding to 2.5% and 97.5% cumulative probability are also shown. To obtain measurement errors nominally the same as those cited in Sect. 4.2 (i.e. associated with finding the line center), we have normalized the deformation distance, Δx, to 10 pixels maximum or approximately 0.35 mm based on the lens magnification. This distance then decreases with the boundary layer profile to zero at the wall. In practice, this is accomplished by selecting the appropriate delay time (Δt in Eq. (3)). As a result, the corresponding time delay at $R_\theta = 1010$ is 1.51 ms, 0.50 ms for $R_\theta = 2870$, and 0.30 ms for $R_\theta = 4850$, for the data presented in Fig. 8b.

Figure 8b presents the magnitude of $\Delta u/u$ across the boundary layer corresponding to the 95% (20:1 odds) confidence interval as indicated in Fig. 8a. As can be seen, the
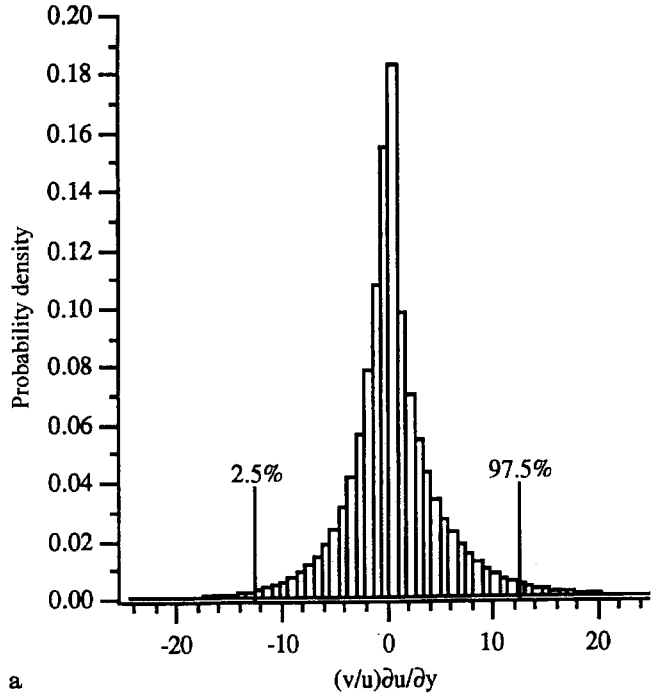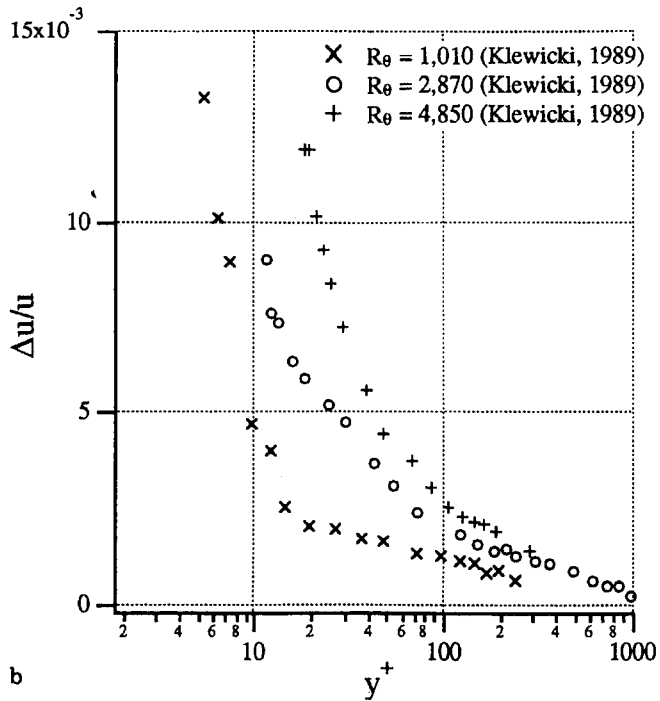
Fig. 8a, b. Probability density function of instantaneous flow angle-velocity gradient product at $y^+ = 15.6$, $R_\theta = 2870$ a; errors resulting from flow tangential to a line in wall-bounded turbulent flows b

error increases in the near wall region. This is due primarily to the large mean gradient. It is worth noting that the error must go to zero at the wall as the wall-normal fluctuations decay more rapidly than the streamwise fluctuations as the wall is approached. Figure 8b also indicates that the error is apparently Reynolds number dependent. This is due primarily to the Reynolds number dependence of the v/u ratio. These data indicate that the instantaneous error due to the flow parallel to the line is small (less than 1.3%) relative to the

measurement errors discussed in Sect. 4.2. As can be seen, this is true throughout the boundary layer. Similar errors are expected in other turbulent flows that are primarily one dimensional in the mean, e.g. jets, wakes, and shear layers. More specifically, in a jet for example, the instantaneous flow angles are approximately 2–3 times those found in a boundary layer, but the maximum velocity gradient is approximately 3–6 times less (assuming U_0 for the jet equals U_∞ for the boundary layer).

4.4
Summary
In addition to the preceding error estimates, some qualitative observations can also be made. The error decreases as the image is magnified, as the error in pixels remains nearly constant. This comes at the expense of reducing the size of the flow region that can be analyzed. If the image magnification becomes very large, curvature effects must (generally) also be accounted for. As the amount of deformation increases, the accuracy increases. This, however, must be done with care to insure that the first order approximation associated with the velocity calculation remains valid. Phosphorescent chemicals yield more accurate results (using the current algorithms) than photochromic chemicals. This is due to the fact that phosphorescent chemicals produce images with greater contrast than photochromic chemicals. With the present algorithms, the line width is only limited by the line spacing. This results in the data reduction being less sensitive to the optical configurations corresponding to different experiments. The errors associated with the delay time and the conversion can be further reduced. These gains, though, will be muted by the fact that the error associated with each of these terms is currently less than one percent, and since the total error (in velocity) is proportional to the sum of the squares of all three terms (including Δx), the 3.5% error in Δx will still dominate. Thus, we are currently working on improvements in our image processing algorithms to reduce this error in Δx. The deformation distance, Δx, effects errors in two ways. For the image processing errors, increasing Δx decreases the percent error. For errors due to the flow parallel to the line however, increasing Δx increases the percent error. These competing effects need to be considered in any given experimental design.

5
Experimental procedure
An experimental program is currently under way to simulate the generation and evolution of coherent vortical motions in the near-wall region of boundary layer flows (Klewicki and Hill 1994). To this end, the following experimental facility is used to produce the desired fluid motions.

5.1
Flow facility
A recirculating liquid flow facility with a 15 cm × 15 cm × 102 cm acrylic test section (Fig. 9) is used. The test section has been modified to accept a surface mounted input device along its lower wall at a distance of 61 cm from the test section inlet. The test section also has four Vicor windows which allow ultraviolet laser light transmission. The working fluid used is a mixture of glycerol and water. Depending on the ratio, this
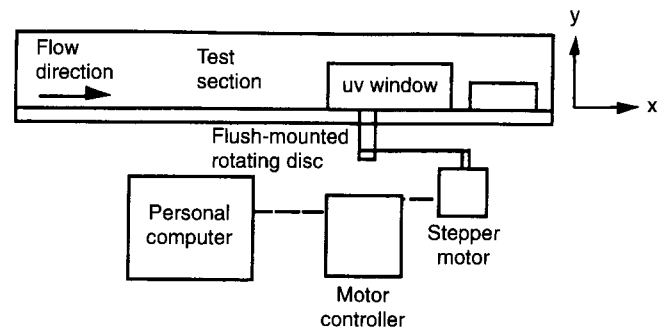

Fig. 9. Test section schematic

mixture has a kinematic viscosity ranging from 10^{-6} to 10^{-3} m²/s. This mixture is also compatible with the chosen photoluminescent chemical, and passes UV light.

5.2
Surface-mounted input device
The surface mounted input device was created to perturb the initially laminar boundary layer with motions ranging from pure rotation to pure strain (or any combination of rotation and strain). Both types of motion are accurately controlled using computer interfaced stepper motors (Fig. 9). The rotational motion actuator is a straightforward gear and gear device. The deformation motion actuator is more complicated, consisting of a piston–cylinder device that is lead-screw driven and connected to the actual input device via tubing and a rotating coupling. For the present experiments, only purely rotational inputs were selected.

The 61 cm fetch upstream of the input device is used to produce a laminar boundary layer which is subsequently perturbed by the rotating disc. This combination, mimics important aspects of motions bearing ω_y in the near-wall region of turbulent boundary layers. This combination also allows a wide variation (in both amplitude and time) of velocity gradient inputs over a wide range of approach boundary layer conditions.

Several characteristics of this flow field preclude the effective use of many measurement techniques. Of primary concern is the ability to measure instantaneous values of velocity and vorticity over planar spatial domains within the flow field. Because of the unsteady behavior of the generated motions, time resolved measurements are needed to track the flow field evolution. Because of the small scale structure of the vorticity field, the spatial resolution of the measurements needs to be good enough to resolve all relevant length scales. Finally, because of the sensitivity of the flow, it is necessary to make the measurements non-intrusively. LIPA meets all of these criteria.

5.3
Data acquisition system for LIPA measurements
The data acquisition system consists primarily of a pulsed excimer laser and a image acquisition system. A Lumonics EX-700 laser is used to excite the photoluminescent chemical (using a typical laser power of 120 mJ/pulse, 10 ns pulse). The image acquisition system consists of an image intensified gated CCD video camera (ITT model F4577) and a high resolu-

tion Panasonic S-VHS video recorder, as well as various synchronization equipment (including a Phillips PM 5712 pulse generator). The external gating capability of the CCD camera allows for synchronization of the camera, laser, and input device via the pulse generator. Delay times associated with each of these devices are at most about 10 μs, giving excellent synchronization. Subsequent post processing and data reduction utilize a Perceptics image capture system in a Macintosh Quandra 900, and a Sparc II workstation.

6
Example results
Results from the current experiments are now briefly discussed. Data from the approach boundary layer and the rotating disk independently are first discussed, followed by interactions involving both. Finally, instantaneous unsteady data are shown from a separate experiment utilizing LIPA and the same data reduction algorithms. These experiments involve the interaction of a shear wake with a circular cylinder.

6.1
Approach boundary layer
The approach boundary layer was quantified using the multiple line LIPA technique discussed earlier. Measurements were made both upstream and downstream of the input device (to determine its effect on the flowfield), along the lower surface of the test section. Interference effects from the disc were negligible. Figure 10 shows the non-dimensional velocity profiles compared with the Blasius solution.

6.2
Rotating disk
The u_θ component velocity profile for the rotating disc (with no boundary layer flow) was quantified using the multiple line LIPA technique with a single line. Figure 11 shows the non-dimensional velocity profiles measured at various radial locations and rotation rates. For clarity, only 5% of the available data for each $\Omega-r$ pair is shown. The data fall on

similarity variables (Von Karman 1921) in the regions not near the edge of the disc. It is interesting to note that for the two rotation rates plotted, the values for δ are 0.48 and 0.62 mm. This demonstrates the excellent spatial resolution of the measurements which would be very difficult to obtain with a single point measurement technique.

6.3
Interaction of boundary layer and rotating disc
Several figures are shown involving data reduced from multiple line LIPA images for flows resulting from the interaction of the approach boundary layer and the flush mounted rotating disk. The emphasis here is on the data itself, rather than the physics of the flowfield. Figure 12 shows two typical axial component velocity fluctuation profiles as a function of distance from the wall, y. These data represent two of 10 lines taken in an $x-y$ plane on the disk centerline imaged from the side view. Figure 13 shows two w component velocity profiles as a function of y. These data are also from a set of 10 lines, but in a $y-z$ plane just downstream of the disk and imaged from the end view. Figure 14 shows u component velocity data as a function of x and z. These data are taken from a series of ten lines in the $x-z$ plane that were nominally parallel to the z axis. They are at a height, $y = 3.0$ mm, and are positioned above the disc (disc center at $x = z = 0$) and imaged from the top view. As indicated in Fig. 14, the velocity shown is the relative velocity; it is the velocity field associated with the combined boundary layer and rotating disc minus the velocity of the boundary layer at $y = 3$ mm. This leads to much more scatter in the data than would be present in an absolute velocity profile, as the errors remain approximately constant (they actually rise slightly as another velocity is calculated), while the scale of the velocity drops by approximately an order of magnitude.
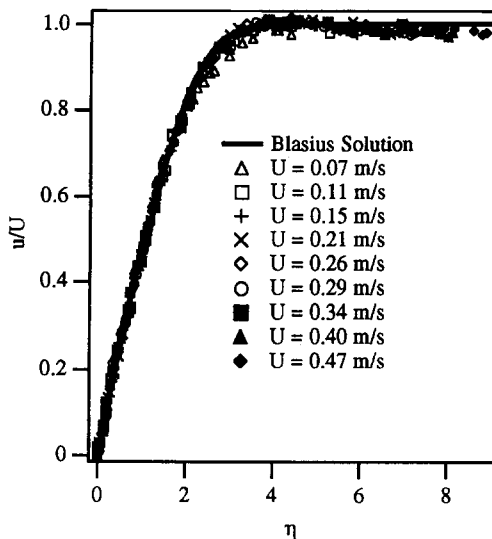
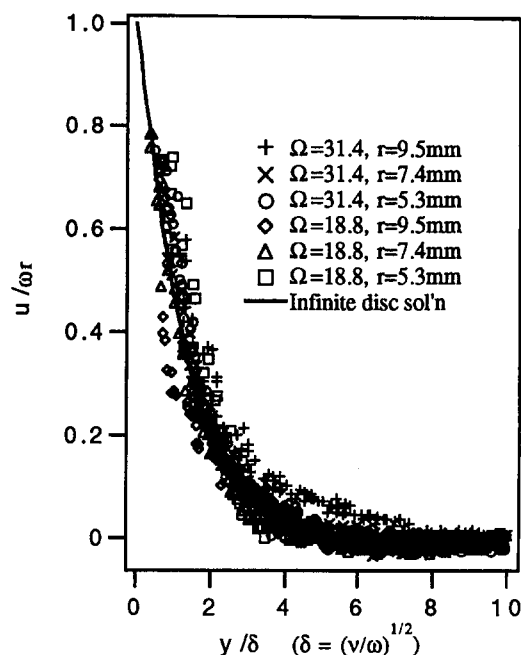Fig. 10. Non-dimensional approach velocity profiles

Fig. 11. Non-dimensional u_θ velocity profiles for rotating disk flow

The quantity of instantaneous spatial velocity information obtained from this technique is quite large. Consider the data of Fig. 14 for example. It is an ensemble average from nine realizations acquired at a single instant in time after the disc motion was initiated. These data come from a larger (time series) data set containing these nine successive realizations at 40 instants in time with 10 lines per frame and 410 individual velocity measurements per line. To generate these data (including optical set-up, data acquisition, and data reduction) took less than two hours.
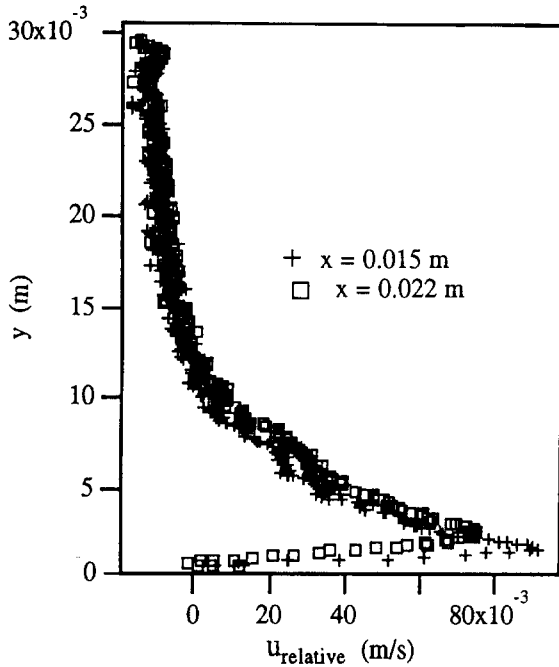
6.4
Interaction of shear wake and circular cylinder

Data are now presented from the study of Lee (1994). This flow, which generates a horseshoe vortex system similar to that observed in boundary layer juncture flows (Baker 1979), has velocities and length scales similar to the laminar boundary layer described above. Figure 15 is a plot of velocity gradient $\partial u/\partial y^*$ (non-dimensionalized by the cylinder diameter and average free stream velocity) as a function of y at different times during an unsteady evolution. These data were generated
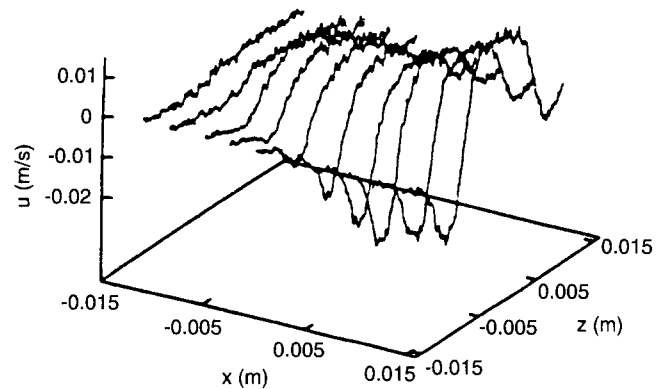
Fig. 12. Relative u component velocity profiles from multiple line measurements

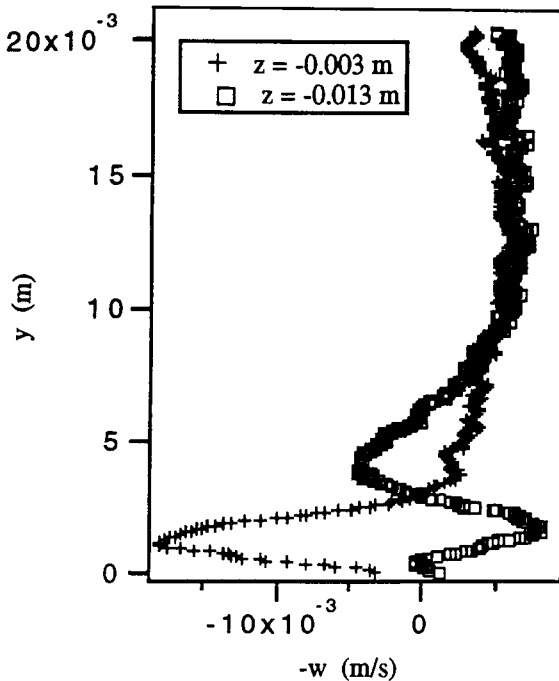Fig. 14. u component (relative) velocity as a function of x and z at a given y location

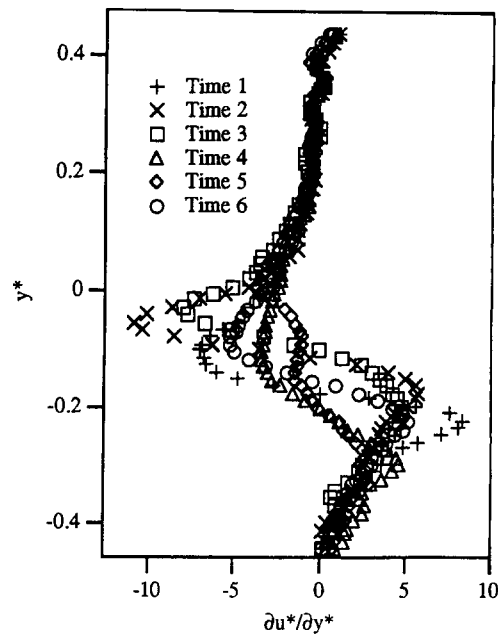Fig. 13. w component velocity profiles from multiple line measurements

Fig. 15. Non-dimensional velocity gradient evolution for shear wake/cylinder interaction. Time step equals 1/3 s
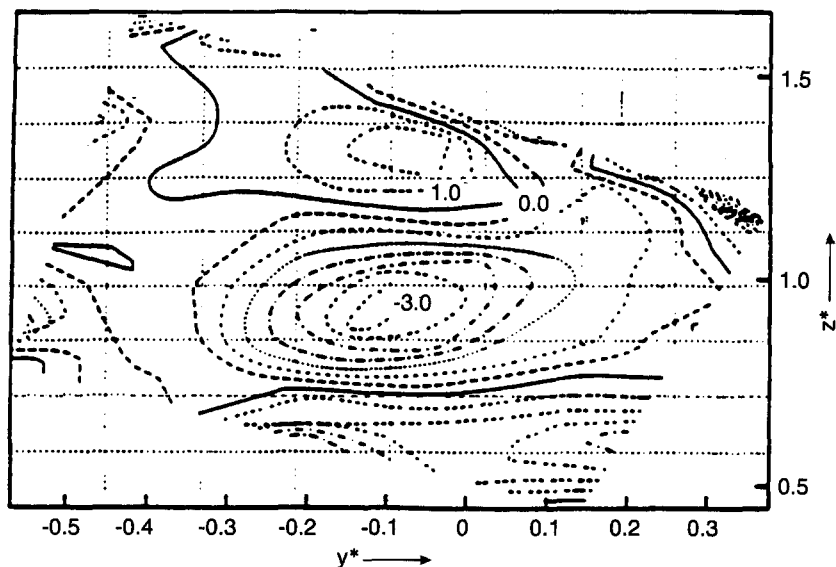
Fig. 16. Non-dimensional streamwise vorticity measurements for shear wake/cylinder interaction

by first finding the u component velocity as a function of y, and then differentiating these profiles. These data are true instantaneous profiles, i.e. no ensembling was used. (Note, to increase the clarity of the plot, only a fraction of the actual data are displayed.) Figure 16 is a plot of streamwise vorticity ω_x^* (again non-dimensionalized by the cylinder diameter and average free stream velocity) as a function of y and z. These data were generated from LIPA grid images as follows. The v and w components of velocity were first found at each grid intersection as discussed previously. From this two component velocity field, the streamwise vorticity could be calculated by two different methods. The first method, which is the method used for these data, is to calculate the derivatives comprising the streamwise vorticity (e.g. $\partial w/\partial y$ and $\partial v/\partial z$) directly from the velocity field data. The second method is to calculate the average vorticity over each grid "box" via the circulation about that box. This method is justified by the small size (typically 1–1.5 mm square) of the grid boxes. A third method for calculating vorticity is currently being explored. This method involves finding the rotation rates of the two lines forming each intersection. Preliminary results are encouraging, but this technique requires the grid lines to be nominally perpendicular.

7
Conclusions

Several advancements to LIPA have been achieved as part of the current experimental program.

1. The use of new, higher quality, photoluminescent chemicals has greatly improved image quality, and thus, data reduction ease and accuracy. The improvements to the image quality include brighter luminescence leading to greater contrast and lower CCD intensifier noise.

2. The image processing algorithms focus on finding a maximum gray scale intensity in a manner similar to Miles et al. (1993). While there are still improvements to be made in the specific subprograms employed, we feel that this method is superior to previous efforts which located the edges of a line and "eroded" this region down to a single pixel width. The error associated with this process is quite strongly related to

the laser line width. Our method is nearly independent of line width, and are thus less dependent on specific experimental conditions.

3. Errors in the instantaneous velocity measurements for multiple lines are shown to be about 3.7% for the data presented here. For other similar experiments, errors are observed to range from approximately 1–7%, depending on the specific experimental parameters. For measurements analyzing only a small region (1.5 cm × 2.0 cm) of the flow, typically, these errors can be reduced by a factor of approximately two. For this case, however, care should be taken, as curvature effects (from the camera and/or lens) may become important. Errors for the grid routines are comparable, as few additional assumptions are made.

4. For a typical multiple line configuration consisting of 10 lines, nearly 1.5 million velocity measurements (nine realizations) can be made every two minutes, after an initial optical setup of approximately one hour. Data reduction to velocity information for these sets of 1.5 million points takes less than one hour on a Sparc II workstation. Single point measurement techniques can not (in a realistic time frame) reproduce these data even at a much coarser resolution.

5. The multiple line technique is shown to provide results with relatively small errors in turbulent boundary layer flows (for streamwise velocity component) at moderate R_θ. Either variation of the LIPA technique should therefore prove to be a valuable measurement tool for understanding turbulence.

References

Baker CJ (1979) The laminar horseshoe vortex. J Fluid Mech 95: 347

Barlow RS; Johnston JP (1985) Structure of turbulent boundary layers on a concave surface. PhD Dissertation, Stanford University, Stanford, CA

Chu CC; Falco RE (1988) Vortex ring/viscous wall layer interaction model of the turbulence production process near walls. Exp Fluids 6: 305

Chu CC; Liao YY (1992) A quantitative study of the flow around an impulsively started cylinder. Exp Fluids 13: 137

Falco RE; Chu CC (1987) Measurement of two-dimensional fluid dynamic quantities using a photochromic grid tracing technique. SPIE 814: 706

Gendrich CP; Koochesfahani MM; Nocera DG (1994) Analysis on molecular tagging velocimetry images for obtaining simultaneous multi-point velocity vectors. Bull Am Phy Soc 39: 1980

Goldfish LH; Koutsky JA; Adler RJ (1965) Chem Engng Sci pp. 1011

Karman T von (1921) Über laminare und turbulente reigung. Z Agnew Math Mech 1: 233–252 (trans. as NACA Tech Mem 1092)

Kim J; Moin P; Moser R (1987) Turbulence statistics in fully developed channel flow at low Reynolds number. J Fluid Mech 177: 133

Klewicki JC (1989) On the interaction between the inner and outer region motions in turbulent boundary layers. PhD Dissertation, Michigan State University, East Lansing, MI

Klewicki JC; Hill RB (1994) Influences of near-wall ω_y on coherent vortex formation. Submitted to ASME Fluids Eng Div Summer Meeting Proceedings, Symp. on Turbulence Control

Lee K (1994) Shear wake interactions with a circular cylinder. PhD Dissertation, University of Utah, Salt Lake City, UT

Lempert W (1992) Private Communication

Miles R; Cohen C; Conners J; Howard P; Huang S; Markovitz E; Russel G (1987) Velocity measurements by vibrational tagging and fluorescent probing of oxygen. Optics Lett 12: 861

Miles RB; Zhou D; Zhang B; Lempert WR; She ZS (1993) Fundamental turbulence measurements by relief flow tagging. AIAA J 31: 447

Miller S (1962) Photochemical reaction for the study of velocity patterns and profiles. BASc Thesis, University of Toronto

Ojha M; Cobbold RSC; Johnston KW; Hummel RL (1989) Pulsatile flow through constricted tubes: an experimental investigation using photochromic tracer methods. J Fluid Mech 203: 173

Ponce A; Wong PA; Way JJ; Nocera DG (1993) Intense phosphorescence triggered by alcohols upon formation of a cyclodextrin ternary complex. J Phys Chem 97: 1137

Popovich AT (1969) Statistical analysis of fluid flow fluctuations in the viscous layer near a solid surface. Ind Engng Chem Fundls 8: 609.

Popovich AT; Hummel RL (1967) A new method for non-disturbing turbulent flow measurement very close to a wall. Chem Engng Sci 22: 21

Popovich AT; Lavallee HC (1970) Flow conditions near roughness elements obtained by photolysis method. Chem Engng Sci 25: 1109

Seeley LE; Hummel RL; Smith JW (1975) Experimental velocity profiles in laminar flow around spheres at intermediate Reynolds numbers. J Fluid Mech 68: 591

Taylor JR (1982) An Introduction to Error Analysis. University Science Books, Mill Valley, CA